THE JOURNAL OF PHYSICAL CHEMISTRY LETTERS
A JOURNAL OF THE AMERICAN CHEMICAL SOCIETY

pubs.acs.org/JPCL

Letter

Chemistry Informed Machine Learning-Based Heat Capacity Prediction of Solid Mixed Oxides

Julian Barra,* Rajni Chahal, Simone Audesse, Jize Zhang, Yu Zhong, Joey Kabel, and Stephen Lam*

Cite This: *J. Phys. Chem. Lett.* 2024, 15, 4721−4728

Read Online

ACCESS | Metrics & More | Article Recommendations | Supporting Information

ABSTRACT: Knowing heat capacity is crucial for modeling temperature changes with the absorption and release of heat and for calculating the thermal energy storage capacity of oxide mixtures with energy applications. The current prediction methods (ab initio simulations, computational thermodynamics, and the Neumann−Kopp rule) are computationally expensive, not fully generalizable, or inaccurate. Machine learning has the potential of being fast, accurate, and generalizable, but it has been scarcely used to predict mixture properties, particularly for mixed oxides. Here, we demonstrate a method for the generalizable prediction of heat capacity of solid oxide pseudobinary mixtures using heat capacity data obtained from computational thermodynamics and descriptors from ab initio databases. Models trained through this workflow achieved an error (mean absolute error of 0.43 J mol^{-1} K^{-1}) lower than the uncertainty in differential scanning calorimetry measurements, and the workflow can be extended to predict other properties derived from the Gibbs free energy and for higher-order oxide mixtures.

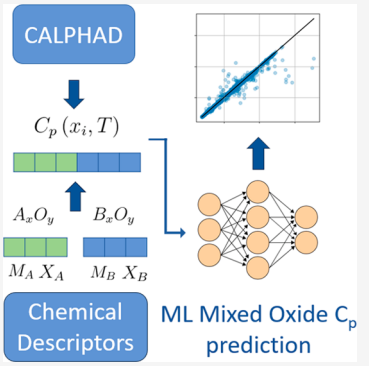

Solid oxide mixtures are increasingly being used in a variety of advanced energy applications. This is owed to the scientific interest and technological potential available in exploring the vast range of oxide mixtures that can be used, allowing for a diverse range of thermophysical, thermodynamic, and electronic properties. This tunability can be leveraged to maximize the performance of energy conversion, energy storage, and renewable energy production systems, which are key in the ongoing decarbonization of electricity grids.[1−6] However, optimizing these properties over a wide range of possible compositions and temperatures, which can exceed 1000 °C for thermal energy storage applications,[7] remains challenging because of our inability to accurately predict the temperature- and composition-dependent properties.

In this study, we explore mixture heat capacity $C_p(T, x)$, a property representing how temperature changes in a mixture in response to absorbed or released heat, which is necessary for modeling the transient thermal behavior of material systems and assessing the performance of thermal devices. Common methods for predicting this property include ab initio simulation, computational thermodynamics (CALPHAD) modeling based on the Gibbs free energy (GFE), and application of simple empirical relations such as the Neumann−Kopp rule (NKR).[8−10] The use of these methods, however, is typically subject to compromise between computational cost and accuracy, which limits their direct application to high-throughput screening and optimization across the composition and temperature ranges. Namely, ab initio methods are generalizable but computationally expensive and are limited to small systems. Here, while the CALPHAD approach is more efficient, it has limited generalizability toward new compositions that lack experimental data because of its semiempirical formulation. Ideal mixing (i.e., NKR) is simple and fast but insufficiently accurate, especially toward higher temperatures. In recent years, machine learning has been shown to be an alternative for material property prediction that circumvents these limitations by providing both accuracy and efficiency. However, most efforts so far have focused on predicting the properties of relatively simple molecules and pure compounds on the basis of their structure.[11−13] As such, a machine learning (ML) framework that allows the prediction of oxide mixture properties from their composition (components and their mole fractions) is still lacking. Here, we propose a methodology for the generalizable prediction of mixture heat capacity using the chemical, structural, and electronic properties of the components (i.e., binary oxide compounds) in the mixture, their mole fractions (x_i, where i represents one component), and temperature as input. The objective of this workflow is to create chemistry-informed prediction models that are more accurate than the NKR, less computationally expensive than ab initio methods, and more generalizable than semiempirical methods over a wide range of compositions and temperatures.

Received: February 16, 2024
Revised: April 5, 2024
Accepted: April 23, 2024
Published: April 25, 2024

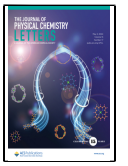

https://doi.org/10.1021/acs.jpclett.4c00506
J. Phys. Chem. Lett. 2024, 15, 4721−4728

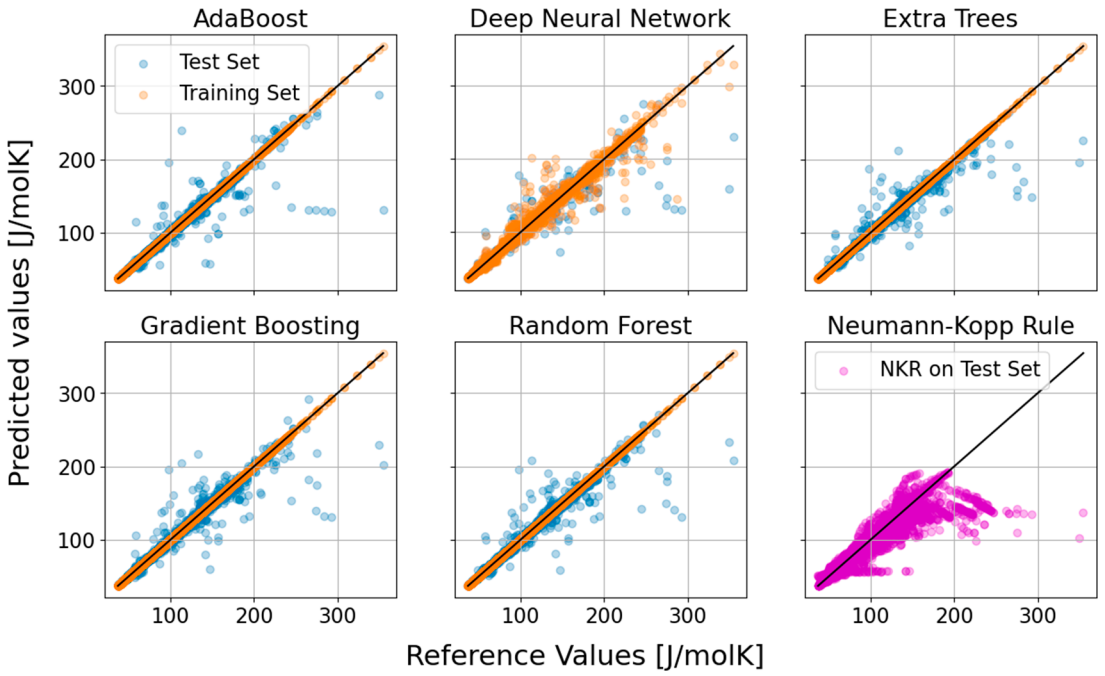

Figure 1. Parity plots (model vs reference) for molar heat capacity () of the training and test sets for AdaBoost (top left), a deep neural network (top middle), extra trees (top right), gradient boosting (bottom left), a random forest (bottom middle), and the empirical NKR (bottom right).

First, a diverse and learnable data set is created for pseudobinary oxides (e.g., A_xO_y-B_wO_z, where A and B are cations and O is oxygen) containing the atomic and structural properties of the mixture components (e.g., A_xO_y) and the corresponding molar heat capacity of a wide range of mixtures. This data set is used to train a variety of ML models, which are compared against the NKR. The heat capacity for the data set is generated utilizing experimentally benchmarked Gibbs free energy models with $C_p = -T\left(\frac{\partial^2 G}{\partial T^2}\right)_{p,Ni}$ [9] These models are based on the compound energy formalism that represents the solution behavior on sublattices that correspond to crystal structure or chemical configurations in solid or liquid solutions.[14] The thermodynamic equilibrium phases and corresponding heat capacities are calculated using CALPHAD software Thermo-Calc with the GFE models implemented in the TCOX12 database.[15] The heat capacity values are generated for 169 pseudobinary oxide systems built from 13 different oxide compounds, at ambient pressure, across the temperatures range of 300−1100 K, and by varying the mole percentage of one of the compounds in the mixture from 0 to 1 in increments of 0.025 mole fraction (the percentage of the other compound is implicit because $x_A + x_B = 1$).

The fractions and temperatures that define this space are included in the data set as input descriptors. To encode chemical information about the components, descriptors obtained from publicly available repositories of ab initio data are included in additional columns. The Materials Project (MP) database[16] and the Jarvis-Tools Classical Force-field Inspired Descriptors (JARVIS-CFID) database[17] are used in this work. In JARVIS-CFID, chemistry−structure−charge information for each compound and its cations is used. JARVIS contains 1557 descriptors for every possible material, and we focus on the subset of the 438 averaged element-based chemical descriptors not feature-engineered from other descriptors available for the material. CFID properties obtained at the compound level represent the average value of that property across all atoms in a molecule. Structure-dependent descriptors are obtained from the MP database as material properties of the minimum energy structure of each compound.[18] The final list of all descriptors included in the data set is available in the Supporting Information.

The data are augmented and preprocessed to ensure permutation invariance of the models and to improve trainability. All chemically equivalent orderings of the same system are added in the training and test data sets. The final data set consists of 108 471 data points ($\{X$ = descriptors for chemical system at specific x_i and T, $Y = C_p\}$), which is split in an 80/20 training/testing ratio. All inputs are standardized using z-scores according to the mean and standard deviations in the training set, and the data are used to tune, train, and evaluate the ML algorithms.[19]

The algorithms tested in this work consist of four decision tree (DT)-based algorithms and a deep neural network (DNN).[20] The DT-based algorithms consist of a random forest (RF),[21] gradient-boosted (GB) regression trees,[22] an AdaBoost (AB)[23] ensemble using DTs as the weak learners, and extra randomized trees (ETs).[24] All DT-based algorithms are tuned by performing 5-fold cross-validation using the mean absolute error (MAE) as the performance metric to tune the maximum depth, number of features, and number of estimators of the base learners, with the final algorithms trained on the entirety of the training set. The last algorithm consists of a fully connected DNN[25] with five hidden layers with 128 nodes each, trained using an Adam optimizer.[26] The DNN is implemented with L2-norm regularization, and hyperparameters are tuned by minimizing the loss on a validation set consisting of 20% of the training set at each epoch.

After training, the feature importance of the descriptors is calculated as the Shapley additive explanation values.[27] These importance values are used to reduce the number of descriptors starting with those that are the least important

https://doi.org/10.1021/acs.jpclett.4c00506
J. Phys. Chem. Lett. 2024, 15, 4721−4728

and are most highly correlated (based on Pearson's correlation coefficient[28]) with other descriptors in the data set. The final data set contains 60 different descriptors per data point (corresponding to the previously mentioned list included in the Supporting Information), and it is used to retrain all models. ML predictions are compared against the CALPHAD-based reference values shown in Figure 1. ML performance metrics are given in terms of mean absolute error (MAE), mean absolute percentage error (MAPE), and coefficient of determination (r^2), and they are compared against the NKR in Table 1.

Table 1. Mean Absolute Errors (MAE), Mean Absolute Percentage Errors (MAPE), and Coefficients of Determination (r^2) of Gradient Boosting (GB), AdaBoost (AB), Random Forest (RF), Extra Trees (ETs), and Deep Neural Network (DNN) Algorithms and the Neumann–Kopp Rule (NKR) for Heat Capacity Prediction in the Test Set

method	MAE (J mol^{-1} K^{-1})	MAPE (%)	r^2
GB	0.65	0.64	0.988
AB	0.69	0.72	0.988
RF	0.60	0.59	0.989
ET	0.43	0.40	0.991
DNN	0.70	0.74	0.988
NKR	2.5	2.2	0.924

Overall, the ML models are highly accurate across all pseudobinary oxide mixtures, with MAPEs ranging from 0.40% to 0.74% (MAE from 0.43 to 0.7 J mol^{-1} K^{-1}), with ET showing the highest prediction accuracy (MAE = 0.43 J mol^{-1} K^{-1}; MAPE = 0.40%; r^2 = 0.991). In all cases, these errors are within the experimental uncertainty of heat capacity measurements through differential scanning calorimetry (~1.5%).[29] Furthermore, all algorithms perform better in the test set than the NKR (MAE = 2.5 J mol^{-1} K^{-1}; MAPE = 2.2%, which is higher than the experimental uncertainty). The NKR shows a smaller error when applied in this data set than other examples of its application in the literature (Kauwe et al.[11] report an MAPE of 13.69% and an r^2 of 0.89, and Gillet et al.[30] report an MAPE of 4–6%). A possible explanation is that these examples predict heat capacity for higher temperatures where the NKR is known to break down (≤3900 K in Kauwe et al. and 2000 K in Gillet et al, contrasting with a maximum temperature of 1100 K in our data set). This highlights performance inconsistencies of empirical or semiempirical models across large thermal and chemical spaces. This is an inherent limitation of a model's expressivity to adequately capture a diverse range of interactions, which can in theory be overcome by ML models. Within the data set presented here, issues in NKR reliability can be clearly seen in the significant deviations that are exhibited in Figure 1 (bottom right). These issues are examined further in the next section.

In addition to the overall MAE, heat capacity $C_p(T, x)$ is predicted for specific oxide systems of technological interest, including NiO, MgO–NiO, Al_2O_3–Cr_2O_3 (the latter two considered for thermal energy storage[31]), CuO–Al_2O_3 (electrocatalysis[32]), Al_2O_3–HfO_2 (dielectrics in light-emitting diodes and solar cells[33,34]), and CuO–HfO_2 (electrochemical reduction of CO_2 into biofuels[35]), as shown in Figure 2. These systems are known to have different solubilities, which allows us to evaluate the ability of the models to predict non-ideal contributions to heat capacity. Here, the $C_p(T, x)$ values predicted by the DNN, ET (smoothest ML predictions, as shown in Figure S1), and NKR are compared for various oxide compositions at temperatures in the range of 300–1100 K.

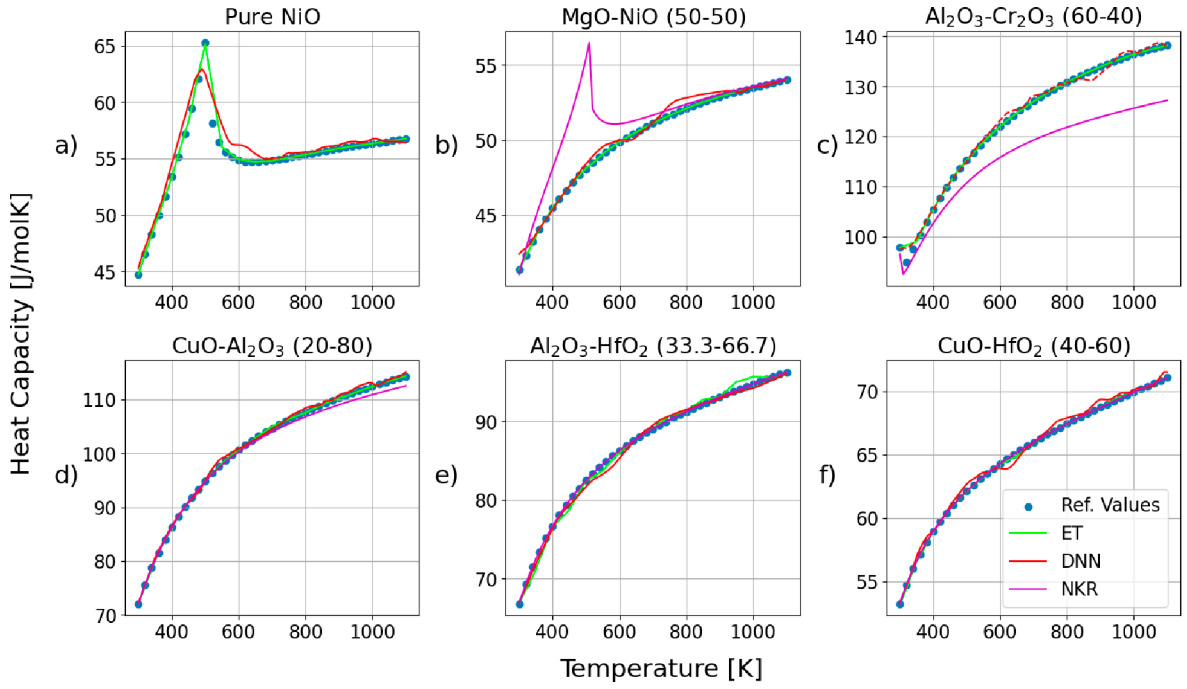

Figure 2. Temperature vs heat capacity curves for selected oxide systems with technological applications: (a) pure NiO, (b) 50 mol %–50 mol % MgO–NiO, (c) 40 mol %–60 mol % Al_2O_3–Cr_2O_3, (d) 20 mol %–80 mol % CuO–Al_2O_3, (e) 33.3 mol %–66.6 mol % Al_2O_3–HfO_2, and (f) 40 mol %–60 mol % CuO–HfO_2. Reference values plotted at a ΔT of 20 K.

https://doi.org/10.1021/acs.jpclett.4c00506
J. Phys. Chem. Lett. 2024, 15, 4721–4728

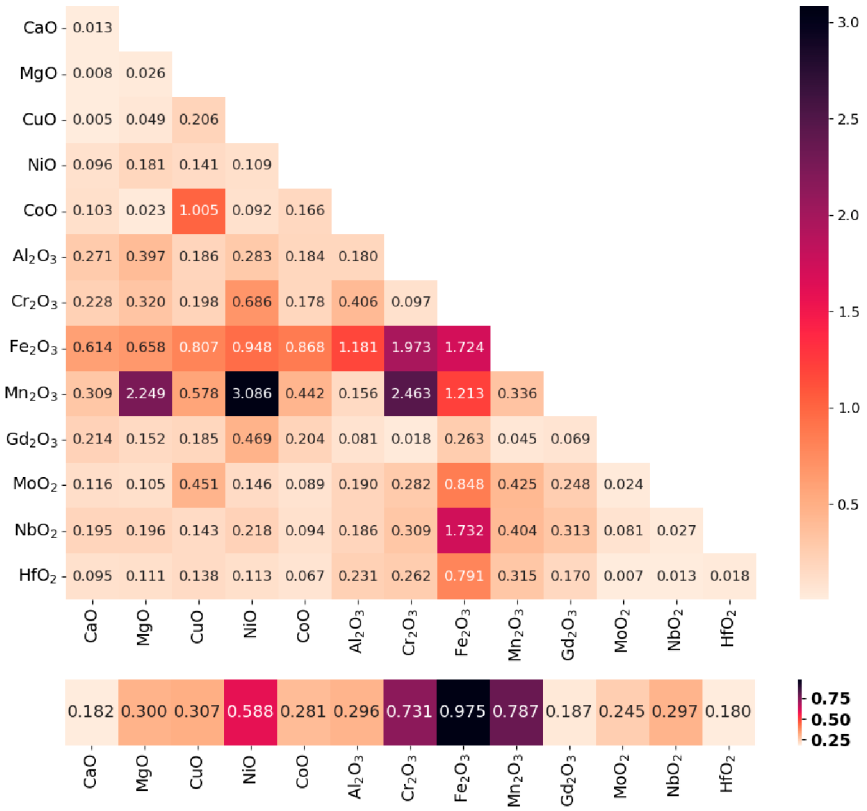

Figure 3. Heat maps showing the performance of the extra trees regressor in terms of MAE of predictions for pseudobinary oxide systems in the test set: (top) matrix showing all combinations of compounds (compound vs compound) and (bottom) matrix showing average MAE across all systems containing a given compound.

For pure NiO (Figure 2a), the ET accurately predicts C_p across the temperature range while the DNN model slightly underpredicts the heat capacity by ∼2 J mol^{-1} K^{-1} around 400−600 K, which exhibits a peak driven by a λ-type transition.[36] When NiO is mixed with MgO, a solid solution is formed (see Figure S1) and the peak disappears as shown in Figure 2b for a 50 mol %−50 mol % NiO−MgO mix. Here, the NKR notably fails due to its assumption of ideal mixing. The NiO−MgO solution is fundamentally different from its components, not featuring the ordered−disordered transition in electron spins that spawn the heat capacity peak in NiO.[37] The inability of NKR to account for this leads to a prediction with the NiO−MgO mix erroneously retaining a peak from pure NiO shown in Figure 2a. In contrast, ML models accurately account for this, suggesting that mixture interactions are accurately captured. The same can be seen in the 60 mol %−40 mol % Al_2O_3−Cr_2O_3 system shown in Figure 2c, which tends toward a single solution at higher temperatures (Figure S2b). For this and other mixtures, the lattice structure of the solution will feature larger bond lengths on average due to short-range repulsive and Coulomb-type interactions, decreasing the vibrational frequency of phonons and increasing the heat capacity.[38,39] As shown in Figure 2c, ML can predict this increase well, whereas the NKR exhibits an increasing error with temperature, underpredicting $C_p(T)$ by ∼12 J mol^{-1} K^{-1} at 1100 K. In other systems with compounds of very different stoichiometries (A:O ratio in each compound), like Al_2O_3−HfO_2 and CuO−HfO_2 shown in panels e and f of Figure 2, respectively, phase segregation occurs, as predicted by CALPHAD (see Figure S2c,d), leading to no contributions of mixing to heat capacity. In these cases, the NKR describes the heat capacity of the system perfectly as expected and the ML methods perform just as accurately, with ET providing the best quantitative and qualitative fit. Namely, ET predictions provide smooth $C_p(T)$ behavior in agreement with the reference data, which is likely due to the inherent resistance to overfitting provided by model ensembling and randomization in the selection of both features and cutoffs. The DNN provides smooth but comparatively less accurate prediction of heat capacity for all systems, with the higher variance of the curve being indicative of overfitting, which could potentially be improved by further regularization and tuning, and a larger data set.

From their predictions on a diverse range of chemical systems (Figure 2), it is apparent that ML models can accurately predict heat capacity data for mixed oxides across the temperature−composition space, regardless of whether mixtures exist as non-ideal solid solutions or multiphase systems. Furthermore, this was achieved without the need to use component-level $C_p(T)$ as model inputs that may not be readily available, making ML models more generalizable than semiempirical methods and more conducive for high-throughput screening across a wide range of compositions and thermodynamic conditions. In this respect, the interpolation accuracy of ML models is examined across all 169 pseudobinary systems in Figure 3. This figure shows the system-averaged MAE in the test set (300−1100 K) for the best performing ML model, ET.

As shown in the heat map matrix in Figure 3 (top), most pseudobinary systems exhibit very small errors below the MAE of 0.433 J mol^{-1} K^{-1} across all systems (Table 1) and the error concentrates in a few systems, including Mn_2O_3−NiO, Cr_2O_3−

https://doi.org/10.1021/acs.jpclett.4c00506
J. Phys. Chem. Lett. 2024, 15, 4721−4728

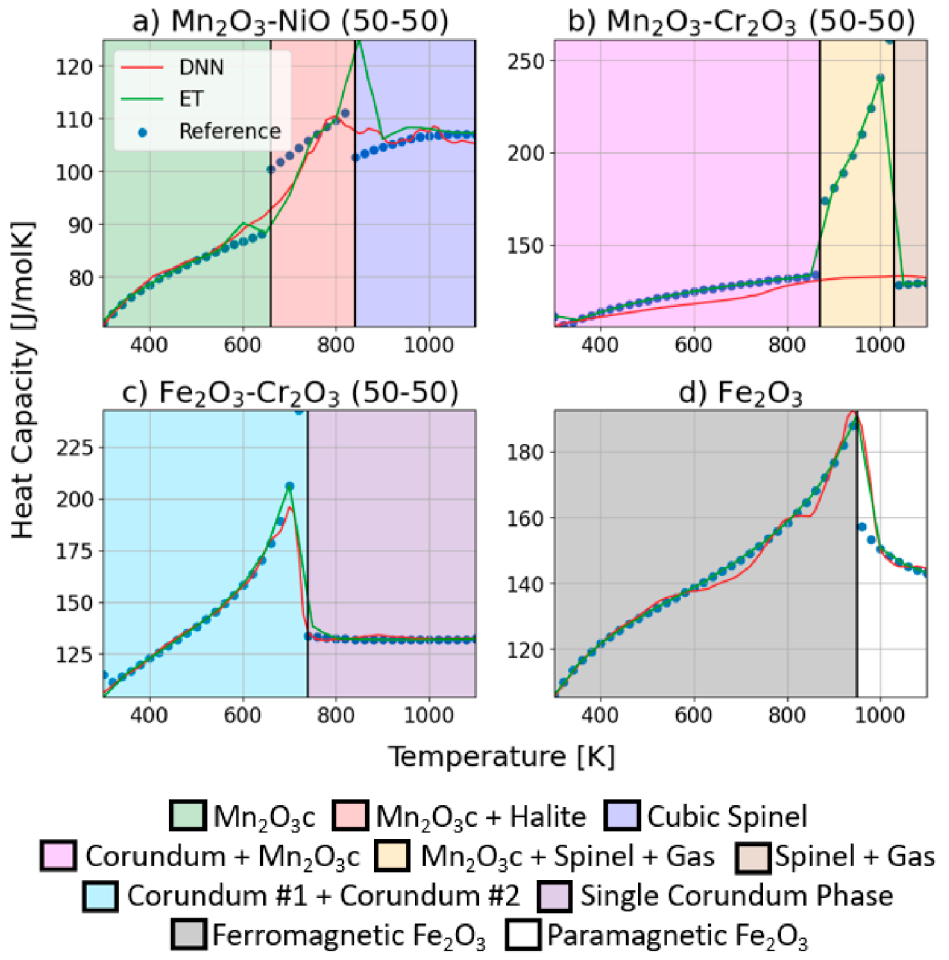

Figure 4. Heat capacity vs temperature with phases overlaid for selected large-error systems: (a) 50 mol %−50 mol % Mn_2O_3−NiO, (b) 50 mol %−50 mol % Mn_2O_3−Cr_2O_3, (c) 50 mol %−50 mol % Fe_2O_3−Cr_2O_3, and (d) pure Fe_2O_3. The different colored regions represent the different phase regions predicted by Thermo-Calc with a legend underneath the plot. The comparison with NKR is shown in Figure S13.

Mn_2O_3, and Cr_2O_3−Fe_2O_3. The bottom part of Figure 3 shows the MAE across each compound, which indicates that systems containing Fe_2O_3 or Mn_2O_3 are generally associated with a larger error of 0.975 or 0.787 J mol^{-1} K^{-1}, respectively. Systems containing NiO and Cr_2O_3 also show large errors (0.588 and 0.731 J mol^{-1} K^{-1}, respectively), but this is mainly associated with the systems that also contain Fe_2O_3 or Mn_2O_3. Not considering these systems produces mean MAEs of 0.211 and 0.290 J mol^{-1} K^{-1}, respectively, which are lower than the overall MAE for ET.

In addition to interpolation, extrapolation toward entirely unseen chemical systems is also tested. First, this is done by excluding components or systems from the training set and testing their performance on those systems as shown in Figures S8−S10. In the Al_2O_3−Cr_2O_3 and CaO tested cases from 300 to 1100 K, the accuracy of ET remains relatively high at MAEs of 4.4 J mol^{-1} K^{-1} (3.5%) and 3.8 J mol^{-1} K^{-1} (6.8%), respectively, which can be reduced further (MAE = 0.66 J mol^{-1} K^{-1}; 1.3%) by addition of a small number (N = 11) of data points (Figure S10). Second, the best-performing ET model is tested against limited experimental data in the NIST-JANAF database, which contains 12 mixed oxide compounds, 11 of them with elements outside of the training data (Li, Na, Be, W, and Ti). Even in this case, the ET provides a remarkable overall prediction accuracy with an MAE of 16.7 J mol^{-1} K^{-1} (MAPE = 10.3%) shown in Figure S12 and details shown in the Supporting Information. This demonstrates the ability of the ML models to learn across the periodic table by drawing on correlations between underlying chemical−structural properties (descriptors) and heat capacity, which cannot be readily inferred by human intuition. Outside of NIST-JANAF (which contains only compounds and not multiphase mixtures), the majority of mixed oxide data exists in commercial databases (e.g., Thermo-Calc, FactSage models fit to experimental data), which should be tested and benchmarked further in future studies.

To better understand the specific behavior of ML models, the predicted $C_p(T)$ is compared to reference data for some of the systems exhibiting the largest errors in Figure 4, including 50 mol %−50 mol % Mn_2O_3−NiO (Figure 4a), 50 mol %−50 mol % Mn_2O_3−Cr_2O_3 (Figure 4b), 50 mol %−50 mol % Fe_2O_3−Cr_2O_3 (Figure 4c), and pure Fe_2O_3 (Figure 4d). Here, the $C_p(T)$ curves are overlaid with the phase regions predicted by CALPHAD.

The results shown in Figure 4 and other calculations in the Supporting Information (Figure S7) suggest that the discontinuities in these curves are the cause of the larger-than-average error. All explored large-error systems present such discontinuities, and calculating MAEs for discontinuous curves gives large errors (ET calculates values of 2.588, 14.351, 3.586, and 0.970 J mol^{-1} K^{-1} for the systems shown in panels a−d, respectively, of Figure 4). Moreover, these discontinuities

https://doi.org/10.1021/acs.jpclett.4c00506
J. Phys. Chem. Lett. 2024, 15, 4721−4728

are characteristic of first- and second-order phase transitions,[37,39] and they are shown to occur at the places at which Thermo-Calc calculates phase transitions of both orders. Those phase transitions are validated when inspecting the experimental phase diagrams and other phase data for the associated systems[40−44] (more details are shown in Section S.5 of the Supporting Information). For the Mn_2O_3−NiO system, Thermo-Calc calculates two phase transitions at 660 and 840 K, which both coincide with the points where discontinuities of ∼12 and ∼9 J mol^{-1} K^{-1}, respectively, appear. The reference value curve shown for the Mn_2O_3−Cr_2O_3 system in Figure 4b shows discontinuities of ∼37 and ∼130 J mol^{-1} K^{-1} that match phase changes calculated through Thermo-Calc perfectly. For 50 mol %−50 mol % Fe_2O_3−Cr_2O_3 (Figure 4c), Thermo-Calc predicts both corundum phases dissolving into a single corundum solute at 740 K, and this roughly matches with the observed heat capacity discontinuity of ∼150 J mol^{-1} K^{-1}. Lastly, Thermo-Calc calculates an unchanging corundum phase across the temperature range for the pure Fe_2O_3 system in Figure 4d, but the discontinuity occurs exactly at the Curie temperature of hematite available through Thermo-Calc and seen in the literature (955.67 and 950 K,[44] respectively), which marks its transition from a ferromagnetic to a paramagnetic material, where a decrease in the heat capacity of ∼34 J mol^{-1} K^{-1} can be seen. In all systems, ML models become less accurate close to the discontinuity points, especially for a DNN, which was unable to capture discontinuities in the Mn_2O_3−Cr_2O_3 system. This is likely due to the continuous functions that are used in DNNs that require more data to provide a better fit around such discontinuities compared to ETs that utilize decision trees. These results suggest that the larger error seen in specific systems is due to phase transitions that cause sharp discontinuities in the mixture heat capacity.

The larger errors exhibited at phase boundaries open two possible avenues for improving the accuracy of the models. The first is to treat the prediction of the heat capacity discontinuities as a more general mathematical problem of approximating discontinuous functions as a topic for which the implementation of neural networks with discontinuous activation functions has been considered.[45] Another option is to incorporate information related to changes and instability in the system phases into the models. There has been work on the prediction of phase diagrams and phase stability using ML methods, which could pave the way for the creation of phase change-informed models for heat capacity prediction,[46,47] which will be explored in the future. Nonetheless, the current ML approach already predicts $C_p(T, x)$ with an error that is less than the experimental uncertainty and state-of-the-art models (ideal, semiempirical), presenting a significant advance and useful tool for the screening and C_p prediction for mixed oxides, which can be generalized to higher-order systems.

In summary, a chemistry-informed ML approach for predicting the heat capacity across a wide range of compositions and temperatures for oxide mixtures has been demonstrated for the first time. The ML models are more accurate than empirical relations, are less computationally expensive than the computational alternatives, and are more generalizable toward unseen compositions, temperatures, and unseen chemical systems, owing to the use of only the chemical−structural data of individual components. It was found that ET is the most accurate of all ML models (MAE = 0.43 J mol^{-1} K^{-1}) and that all ML models can predict the excess heat capacity resulting from molecular interactions in oxide mixtures, enabling high-throughput screening. Although larger errors were concentrated in systems exhibiting discontinuities in $C_p(T)$ at phase boundaries, this can be improved in the future with advanced NN architectures that handle discontinuities, or phase-informed descriptors. The approach demonstrated by this work can be readily extended to the prediction of other GFE-derived mixed oxide properties (e.g., density, thermal expansion coefficient, etc.) and other solid mixtures in general.

■ ASSOCIATED CONTENT

Supporting Information

The Supporting Information is available free of charge at https://pubs.acs.org/doi/10.1021/acs.jpclett.4c00506.

List of descriptors included in the data set, selection of models for smooth heat capacity prediction, moles of phases versus temperature, experimental phase diagrams from the literature, heat capacity versus temperature and experimentally assessed phases, transferability of machine learning models, computational expense of CALPHAD and ML models, and NKR performance in large-error systems (PDF)

Transparent Peer Review report available (PDF)

■ AUTHOR INFORMATION

Corresponding Authors

Julian Barra − *Department of Chemical Engineering, University of Massachusetts Lowell, Lowell, Massachusetts 01854, United States;* orcid.org/0009-0008-2834-2973; Email: Julian_BarraOtondo@student.uml.edu

Stephen Lam − *Department of Chemical Engineering, University of Massachusetts Lowell, Lowell, Massachusetts 01854, United States;* orcid.org/0000-0002-7683-1201; Email: Stephen_Lam@uml.edu

Authors

Rajni Chahal − *Oak Ridge National Laboratory, Oak Ridge, Tennessee 37830, United States;* orcid.org/0000-0003-2190-0473

Simone Audesse − *Department of Chemical Engineering, University of Massachusetts Lowell, Lowell, Massachusetts 01854, United States*

Jize Zhang − *Mechanical and Materials Engineering, Worcester Polytechnic Institute, Worcester, Massachusetts 01609, United States*

Yu Zhong − *Mechanical and Materials Engineering, Worcester Polytechnic Institute, Worcester, Massachusetts 01609, United States*

Joey Kabel − *Electrified Thermal Solutions, Inc., Medford, Massachusetts 02155, United States*

Complete contact information is available at: https://pubs.acs.org/10.1021/acs.jpclett.4c00506

Notes

The authors declare no competing financial interest.

■ ACKNOWLEDGMENTS

J.B., R.C., S.A., and S.L. acknowledge funding from National Science Foundation Grant 2138456.

REFERENCES

(1) Samira, S.; Gu, X. K.; Nikolla, E. Design Strategies for Efficient Nonstoichiometric Mixed Metal Oxide Electrocatalysts: Correlating Measurable Oxide Properties to Electrocatalytic Performance. *ACS Catal.* **2019**, *9*, 10575−86.

(2) Kim, J. Y.; Lee, J. W.; Jung, H. S.; Shin, H.; Park, N. G. High-Efficiency Perovskite Solar Cells. *ACS Chem. Rev.* **2020**, *120*, 7867−918.

(3) André, L.; Abanades, S.; Cassayre, L. High-Temperature Thermochemical Energy Storage Based on Redox Reactions Using Co-Fe and Mn-Fe Mixed Metal Oxides. *J. Solid State Chem.* **2017**, *253*, 6−14.

(4) Forsberg, C.; Peterson, P. F. Basis for Fluoride Salt-Cooled High-Temperature Reactors with Nuclear Air-Brayton Combined Cycles and Firebrick Resistance-Heated Energy Storage. *Nucl. Technol.* **2016**, *196*, 13−33.

(5) Ziegler, M. S.; Mueller, J. M.; Pereira, G. D.; Song, J.; Ferrara, M.; Chiang, Y. M.; Trancik, J. E. Storage Requirements and Costs of Shaping Renewable Energy Toward Grid Decarbonization. *Joule* **2019**, *3*, 2134−53.

(6) Dowling, J. A.; Rinaldi, K. Z.; Ruggles, T. H.; Davis, S. J.; Yuan, M.; Tong, F.; Lewis, N. S.; Caldeira, K. Role of Long-Duration Energy Storage in Variable Renewable Electricity Systems. *Joule.* **2020**, *4*, 1907−28.

(7) Stack, D. C.; Curtis, D.; Forsberg, C. Performance of Firebrick Resistance-Heated Energy Storage for Industrial Heat Applications and Round-Trip Electricity Storage. *Appl. Energy.* **2019**, *242*, 782−96.

(8) Stoffel, R. P.; Wessel, C.; Lumey, M. W.; Dronskowski, R. Ab Initio Thermochemistry of Solid-State Materials. *Angew. Chem., Int. Ed.* **2010**, *49*, 5242−66.

(9) Lukas, H. L.; Fries, S. G.; Sundman, B. *Computational Thermodynamics: The CALPHAD Method*; Cambridge University Press: New York, 2007.

(10) Leitner, J.; Voňka, P.; Sedmidubský, D.; Svoboda, P. Application of Neumann-Kopp Rule for the Estimation of Heat Capacity of Mixed Oxides. *Thermochim. Acta* **2010**, *497*, 7−13.

(11) Kauwe, S. K.; Graser, J.; Vazquez, A.; Sparks, T. D. Machine Learning Prediction of Heat Capacity for Solid Inorganics. *Integr. Mater. Manuf. Innov.* **2018**, *7*, 43−51.

(12) Juneja, R.; Yumnam, G.; Satsangi, S.; Singh, A. K. Coupling the High-Throughput Property Map to Machine Learning for Predicting Lattice Thermal Conductivity. *Chem. Mater.* **2019**, *31*, 5145−5151.

(13) Tewari, A.; Dixit, S.; Sahni, N.; Bordas, S. P. A. Machine Learning Approaches to Identify and Design Low Thermal Conductivity Oxides for Thermoelectric Applications. *Data-Centric Engineering* **2020**, *1*, No. e8.

(14) Hillert, M. The Compound Energy Formalism. *J. Alloys Compd.* **2001**, *320*, 161−176.

(15) *Thermo-Calc Software. TCS Metal Oxide Solutions Database (TCOX12)*; 2022. https://thermocalc.com/ (accessed 2024-05-04).

(16) Jain, A.; Ong, S. P.; Hautier, G.; Chen, W.; Richards, W. D.; Dacek, S.; Cholia, S.; Gunter, D.; Skinner, D.; Ceder, G.; Persson, K. A. Commentary: The Materials Project: a Materials Genome Approach to Accelerating Materials Innovation. *APL Mater.* **2013**, *1*, 1.

(17) Choudhary, K.; Garrity, K. F.; Reid, A. C. E.; DeCost, B.; Biacchi, A. J.; Hight Walker, A. R.; Trautt, Z.; Hattrick-Simpers, J.; Kusne, A. G.; Centrone, A.; Davydov, A.; Jiang, J.; Pachter, R.; Cheon, G.; Reed, E.; Agrawal, A.; Qian, X.; Sharma, V.; Zhuang, H.; Kalinin, S. V.; Sumpter, B. G.; Pilania, G.; Acar, P.; Mandal, S.; Haule, K.; Vanderbilt, D.; Rabe, K.; Tavazza, F. The Joint Automated Repository for Various Integrated Simulations (JARVIS) for Data-Driven Materials Design. *npj Comput. Mater.* **2020**, *6*, 173.

(18) Bartel, C. J. Review of Computational Approaches to Predict the Thermodynamic Stability of Inorganic Solids. *J. Mater. Sci.* **2022**, *57*, 10475−98.

(19) Pearson, R. K. Outliers in Process Modeling and Identification. *IEEE Trans. Control Syst. Technol.* **2002**, *10*, 55−63.

(20) Hinton, G. E. Connectionist Learning Procedures. *Artif. Intell.* **1989**, *40*, 185−234.

(21) Breiman, L. Random Forests. *Mach. Learn.* **2001**, *45*, 5−32.

(22) Friedman, J. H. Greedy Function Approximation: a Gradient Boosting Machine. *Annals of Statistics* **2001**, *29*, 1189−1232.

(23) Drucker, H. Improving Regressors Using Boosting Techniques. *ICML* **1997**, 107−115.

(24) Geurts, P.; Ernst, D.; Wehenkel, L. Extremely Randomized Trees. *Mach. Learn.* **2006**, *63*, 3−42.

(25) Murtagh, F. Multilayer Perceptrons for Classification and Regression. *Neurocomputing.* **1991**, *2*, 183−197.

(26) Zeiler, M. D. ADADELTA: An Adaptive Learning Rate Method. *arXiv* **2012**, DOI: 10.48550/arXiv.1212.5701.

(27) Lundberg, S. M.; Allen, P. G.; Lee, S. I. A Unified Approach to Interpreting Model Predictions. *arXiv* **2017**, DOI: 10.48550/arXiv.1705.07874.

(28) Pearson, K. Note on Regression and Inheritance in the Case of Two Parents. *Proc. R. Soc. London* **1895**, *58*, 240−242.

(29) Rudtsch, S. Uncertainty of Heat Capacity Measurements with Differential Scanning Calorimeters. *Thermochim. Acta* **2002**, *382*, 17−25.

(30) Gillet, P.; Richet, P.; Guyot, F.; Fiquet, G. High-Temperature Thermodynamic Properties of Forsterite. *J. Geophys. Res.* **1991**, *96*, 11805−11816.

(31) Stack, D. C. Development of High-Temperature Firebrick Resistance-Heated Energy Storage (FIRES) Using Doped Ceramic Heating System. Ph.D. Thesis, Massachusetts Institute of Technology, Cambridge, MA, 2021.

(32) Mujtaba, A.; Janjua, N. K. Fabrication and Electrocatalytic Application of CuO@Al_2O_3 Hybrids. *J. Electrochem. Soc.* **2015**, *162*, H328−H337.

(33) Xu, Y.; Chen, H.; Xu, H.; Chen, M.; Zhou, P.; Li, S.; Zhang, G.; Shi, W.; Yang, X.; Ding, X.; Wei, B. Physical Properties of an Ultrathin Al_2O_3/HfO_2 Composite Film by Atomic Layer Deposition and the Application in Thin-Film Transistors. *ACS Appl. Mater. Interfaces.* **2023**, *15*, 16874−81.

(34) Smirnova, T. P.; Lebedev, M. S.; Morozova, N. B.; Semyannikov, P. P.; Zherikova, K. V.; Kaichev, V. V.; Dubinin, Y. V. MOCVD and Physicochemical Characterization of $(HfO_2)_x$-$(Al_2O_3)_{1-x}$ Thin Films. *Chem. Vap. Depos.* **2010**, *16* (16), 185−90.

(35) Li, X.; Li, L.; Wang, L.; Xia, Q.; Hao, L.; Zhan, X.; Robertson, A. W.; Sun, Z. Engineering the CuO-HfO_2 Interface Toward Enhanced CO_2 Electroreduction to C_2H_4. *ChemComm.* **2022**, *58*, 7412−5.

(36) Radwanski, R. J.; Ropka, Z. Specific Heat and the Ground State of NiO. *Acta Phys. Polym.* **2008**, *114*, 213.

(37) Thorn, R. J. On the Origin of the Lambda-Type Transition in Heat Capacity. *J. Chem. Thermodyn.* **2002**, *34*, 973−85.

(38) Benisek, A.; Dachs, E. On the Nature of the Excess Heat Capacity of Mixing. *Phys. Chem. Miner.* **2011**, *38*, 185−91.

(39) Kittel, C.; Kroemer, H. *Thermal Physics*, 2nd ed.; W. H. Freeman and Co.: New York, 1980.

(40) Wickham, D. G. Solid-Phase Equilibria in the System NiO-Mn_2O_3-O_2. *J. Inorg. Nucl. Chem.* **1964**, *26*, 1369−77.

(41) Speidel, D. H.; Muan, A. The System Manganese Oxide - Chromium Oxide in Air. *J. Am. Chem. Soc.* **1963**, *46*, 577−578.

(42) Muan, A.; Omiya, S. Phase Relations in the System Iron Oxide - Chromium Oxide in Air. *J. Am. Chem. Soc.* **1960**, *43*, 204−209.

(43) Benny, S.; Grau-Crespo, R.; De Leeuw, N. H. A Theoretical Investigation of α- Fe_2O_3-Cr_2O_3 Solid Solutions. *Phys. Chem. Chem. Phys.* **2009**, *11*, 808−815.

(44) Sakurai, S.; Namai, A.; Hashimoto, K.; Ohkoshi, S. I. First Observation of Phase Transformation of All Four Fe_2O_3 Phases ($\gamma \rightarrow \varepsilon \rightarrow \beta \rightarrow \alpha$-Phase). *J. Am. Chem. Soc.* **2009**, *131*, 18299−18303.

(45) Della Santa, F.; Pieraccini, S. Discontinuous Neural Networks and Discontinuity Learning. *J. Comput. Appl. Math.* **2023**, *419*, No. 114678.

(46) Lund, J.; Wang, H.; Braatz, R. D.; García, R. E. Machine Learning of Phase Diagrams. *Mater. Adv.* **2022**, *3*, 8485−8497.

https://doi.org/10.1021/acs.jpclett.4c00506
J. Phys. Chem. Lett. 2024, 15, 4721−4728

(47) Arróyave, R. Phase Stability Through Machine Learning. *J. Phase Equilibria and Diffus.* **2022**, *43*, 606−28.

https://doi.org/10.1021/acs.jpclett.4c00506
J. Phys. Chem. Lett. 2024, 15, 4721−4728